Title

Corrective receding horizon EV charge scheduling using short-term solar forecasting

Journal

Renewable Energy, 130(C)

ISSN

0960-1481

Authors

Wang, Guang Chao
Ratnam, Elizabeth
Haghi, Hamed Valizadeh
et al.

Publication Date

2019

DOI

10.1016/j.renene.2018.08.056

Peer reviewed

Corrective Receding Horizon EV Charge Scheduling Using Short-Term Solar Forecasting

Guang Wang[a], Elizabeth Ratnam[b], Hamed Valizadeh Haghi[a], Jan Kleissl[a]
[a] Center for Renewable Resources and Integration, Department of Mechanical and Aerospace Engineering, University of California, San Diego
[b] Berkeley Energy and Climate Institute, Department of Electrical Engineering and Computer Science, University of California, Berkeley

Abstract— Forecast errors can cause sub-optimal solutions in resource planning optimization, yet they are usually modeled simplistically by statistical models, causing unrealistic impacts on the optimal solutions. In this paper, realistic forecast errors are prescribed, and a corrective approach is proposed to mitigate the negative effects of day-ahead persistence forecast error by short-term forecasts from a state-of-the-art sky imager system. These forecasts preserve the spatiotemporal dependence structure of forecast errors avoiding statistical approximations. The performance of the proposed algorithm is tested on a receding horizon quadratic program developed for valley filling the midday net load depression through electric vehicle charging. Throughout one month of simulations the ability to flatten net load is assessed under practical forecast accuracy levels achievable from persistence, sky imager and perfect forecasts. Compared to using day-ahead persistence solar forecasts, the proposed corrective approach using sky imager forecasts delivers a 25% reduction in the standard deviation of the daily net load. It is demonstrated that correcting day-ahead forecasts in real time with more accurate short-term forecasts benefits the valley filling solution.

Keywords: Electric vehicle charging; Optimal scheduling; Solar forecast errors

1. Introduction

1.1 Problem Statement and Literature Review

The variable nature of solar power is of concern to electric grid operators, where there is substantial growth in photovoltaic (PV) installations. Variable power flow occurs primarily due to passing clouds. As a result, PV generation exhibits high variability, leading to power quality issues such as flicker, power imbalance, reverse power flow, and increased wear on conventional voltage regulator equipment at the distribution level [1, 2]. With high PV penetration, these effects aggravate and can cause challenges to grid operations.

Accurate solar forecasts help grid operators integrate increased levels of solar generation while maintaining power quality. However, forecast errors are inherent to any forecasting technique, and non-linear atmospheric dynamics make it challenging to reduce or correct solar forecast errors. Forecast errors can be detrimental to reduce peak loads using energy storage [3-5], or maximizing PV self-consumption [6]. While the characteristics of forecast errors vary with time scale and location [7, 8], grid integration studies typically model forecast errors by two main approaches:

i. Generate an imperfect forecast by adding a synthetic error to the actual solar generation. The synthetic error is often sampled from univariate distributions such as Gaussian, uniform, and Weibull [9-14]. Such error timeseries have zero autocorrelation, failing to capture the autocorrelation properties of real forecast errors. Days with large forecast error autocorrelation, especially persistent over-forecasts for several hours, usually present the most challenging conditions for energy storage to reduce peak load [15]. On such days the energy storage system needs to discharge continuously to make up for the shortfall in PV generation which may cause premature discharge, demand peaks, and associated demand charges.

ii. Probabilistic modeling of errors: sophisticated statistical methods such as copula functions [16], Markov model [17], enhanced Markov chain model [18] and kernel density estimation [19] are utilized to model the time series forecast. However, these models do not fully capture the autocorrelation of forecast errors due to nonlinear and higher order dependencies. For example, the transformation-based heuristic methodology in [20] captures the spatio-temporal correlation properties of forecast errors on the day-ahead time scale, but not intra-day. Other forecast error modeling considering autocorrelation include [15] where a parametric first-order autoregressive process is developed to generate autocorrelated time series forecasts and [21] where a simulated autocorrelated PV forecast error through a transformed multivariate ARMA model is presented.

1.2 Objectives and Contribution

While modeling forecast errors to support grid planning and operation studies has received much attention, corrections of the impact of forecast errors in real time are typically not applied. Motivated by this, we propose a corrective approach with the main contributions listed as follows:

i. We avoid statistical models of forecast errors by using a day-ahead persistence and 15 min-ahead sky imager forecast to produce real forecast data which inherently preserves the temporal dependence structure of forecast errors.

ii. We apply a corrective optimization framework. The baseline day-ahead persistence forecast is corrected by three short-term forecasts showcasing different levels of realistic forecast errors: day-ahead perfect forecasts, day-ahead persistence forecasts corrected by imperfect short-term sky imagery forecasts, and day-ahead persistence forecasts corrected by perfect short-term forecasts. This approach captures the real forecast property of improved accuracy with shorter forecast horizon.

The proposed case study to implement and validate the above framework uses EVs as mobile energy storage systems (ESS). Adopting ESS to compensate the mismatch between variable PV output and grid load [22, 23] has been extensively studied in the past decade. For example, Nottrott et al. [24] modeled ESS dispatch schedules for peak net load minimization by linear programming. Mixed-integer linear programming and quadratic programming are also commonly utilized to solve the ESS scheduling problem at the distribution level [25-28]. The adoption of EV as an alternative to ESS has received significant attention [29] because of low acquisition cost. The interaction between EVs and the power grid is comprehensively discussed in [30]. High EV penetration can provide grid services [31] such as valley filling defined as increasing load demand during the load depression [32] using unidirectional EV charging management (V1G) [33] or vehicle-to-grid (V2G) [34] schemes. We formulate a typical valley filling problem through centralized [35] EV charge scheduling in a realistic, quasi-operational case study. Since V2G still faces challenges such as market barriers and limited commercial availability we focus on V1G here. The impact of realistic forecast errors is quantified as the deviation of the resulting valley filling solution from the ideal solution. Last, we illustrate how correcting day-ahead forecasts in real time with more accurate short-term forecasts benefits the valley filling solution.

1.3 Paper Organization

The remainder of this paper is organized as follows. In Section 2 we introduce the methodology for determining load demand, solar forecasts, and EV charge events. Section 3.1 defines the problem statement, and sections 3.2 and 3.3 introduce a quadratic programming (QP) optimization algorithm based on [28]. We extend the work by supplementing constraints for start and end time of EV charging and energy demand satisfaction, and integrating a receding horizon framework. Section 3.4 introduces error metrics. Section 4.1-4.2 provide a validation on a sample day, and statistical results from one month of valley filling results, and the discussion of the results and limitations of the proposed methodology are given in Section 4.3-4.4. Lastly, Section 5 provides conclusions and future work.

2. Problem setup and System Data

2.1 Geographic Setup

We select the region of San Bernardino located in Southern California, where Southern California Edison (SCE) installed 125 MW of multiple rooftop photovoltaic (PV) systems under the Solar Photovoltaic Program (SPVP) [36]. This region is home to many commercial buildings, large warehouses, and abundant solar resources, which makes large PV rooftop arrays common. Local distribution feeders are therefore prone to solar variability issues, making this region an ideal location for solar power

integration studies.

Figure 1 shows an overview of the area served by the 66/12 kV substation in San Bernardino, CA. The substation load demand was simulated by EnergyPlus, a building energy simulation tool developed by the U.S. Department of Energy. Power output from two SPVP systems were provided by SCE. To produce short-term solar forecasts, we use a UC San Diego Sky Imager system (USI). The USI is rooftop-mounted and its field-of-view covers all buildings within the substation service territory. It can be used to geolocate clouds, measure cloud velocity, and track cloud motion [37, 38]. These measurements are then used to predict future cloud shadow locations and solar irradiance up to 15 min ahead. For more detailed information of solar resource assessment and forecasting using the USI, refer to [39, 40].

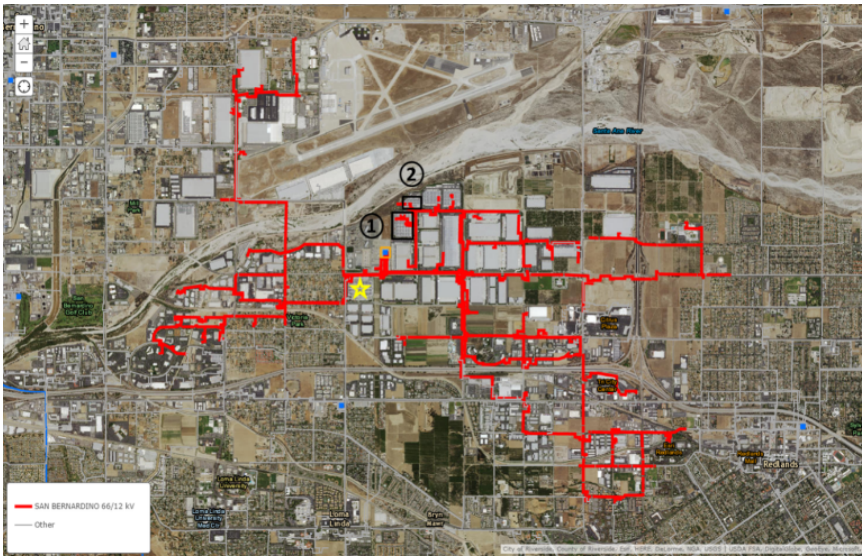

Figure 1: Southern California Edison's (SCE) Distributed Energy Resource Interconnection Map (DERiM) showing the San Bernardino substation service territory. The substation is marked by a blue box with orange border and feeder lines emanating from that substation are in red. Rooftop PV systems (black boxes) and sky imager (yellow star) are located up to 1,100 m apart. The map spans 12 x 6.5 km.

2.2 Solar Forecasts

To demonstrate the net load flattening improvement through correcting day-ahead persistence forecast by short-term forecast updates, we construct four different solar generation forecasts G in 24-hour time windows representing different forecast accuracy through a combination of persistence G_{p}, USI G_{USI}, and perfect forecast G_{perfect}.

1. Base Forecast (G_{p}): As conventionally adopted [3, 41] as a baseline for load forecasting, a 24-hour persistence forecast is defined as solar power at the same time of the previous day. Persistence forecasts are expected to have the largest forecast error and largest autocorrelation of forecast errors.

2. Operational forecasts ($G_{\mathrm{p+USI}}$): The base forecast is continually updated with the most recent USI forecast. Since USI forecast horizons are limited to 15 min, only the G_{p} in the first 15 min of the 24-hour time horizon is replaced with G_{USI} while the G_{p} in the remaining time horizons are left unchanged. As G_{USI} is more accurate than G_{p} (refer to Table A-2 in the Appendix), $G_{\mathrm{p+USI}}$ is expected to exhibit smaller forecast errors than G_{p}.

3. Benchmark forecast ($G_{\mathrm{p+perfect}}$): Similar to the operational forecast, but the first 15 min of G_{p} is replaced with G_{perfect} . $G_{\mathrm{p+perfect}}$ is expected to exhibit even smaller forecast errors than the operational forecast. Thus it elucidates whether further improvements in the accuracy of short-term forecast would result in better mitigating the impact of forecast errors on the net load.

4. Perfect Forecast (G_{perfect}): The entire 24-hour time horizon of G_{p} is replaced with G_{perfect}, yielding zero forecast error. The perfect forecast brackets the net load flattening that is achievable. If EV availability was unconstrained, G_{perfect} would yield a flat net load curve.

2.3 EV Fleet

We focus on workplace charging of EVs during regular business hours coinciding with times of peak PV production. A fleet of EVs connected to workplace charging stations is simulated. The EV make and models and their battery capacity and charge rates are selected based on the EV market share in the US as of 2015 (Table A-1).

Arrival time, layover duration, and the initial state of charge were sampled from the following distributions: 1) EV arrival time varies between 06:00 PST and 10:00 PST centered on a mean arrival time of 07:30 PST with a standard deviation of 1 h. 2) layover duration spans from 6 to 11 hours centered on 8 hours with a standard deviation of 1 h. 3) initial state of charge (χ_0, in %) ranges from 0-100% centered on 60% with a standard deviation of 10%. The energy demand is derived assuming a full charge by the departure time. The resulting EV charging events are replicated for all 30 days of analysis. Since most employee day-to-day schedules are repetitive, the persistence of daily charging events is a reasonable assumption.

2.4 Summary of Data Sources and Availability

Table 1 provides an overview of the load, PV generation, and EV energy demand datasets. Because PV generation data is complete only for April 2013, the full month is selected for our analysis. During this month, there were 2 overcast days, 13 clear days, and the remaining 15 days were partly cloudy. The simulated substation loads were scaled down by a factor of 150x from 5.4 MW to 36 kW and PV data were also scaled down by 75x from 7.5MW to 100 kW so that the 31 EVs in Table A-1 are able to fill the entire energy valley on a clear day.

Table 1: Catalog of the datasets and their native temporal resolution. All data are interpolated to 15 min temporal resolution. The rated EV charge capacity is determined by the sum of the charge rates in Table A-1.

Data Source	Rated Capacity	Scale Factor	Average Daily Power	Type	Original Time Resolution
Loads	5.4 MW	150	23 kW	Simulated	60 min
PV Generation	7.5 MW	75	13 kW	Measured	30 s to 2 min, irregularly spaced
USI PV Forecast	7.5 MW	75	13 kW	Measured Sky Images	30 sec
EV Charge Capacity	0.23 MW	1	19 kW	Simulated	5 min

3. Methodology

3.1 Problem Setup

To test our proposed approach, we formulate a valley filling optimization problem to schedule EV charging. Figure 2 schematically illustrates the problem configuration. The load demand estimate L for all buildings connected to the distribution feeder is offset by PV systems injecting power G. The substation is assumed to allow bidirectional power flow (i.e. net load NL, positive if delivering power and negative for reverse power flow). N EVs draw charge power $\beta^{[N]}$ from the distribution grid. The arrowheads indicate positive power flow. As V2G (i.e. Vehicle to Grid charging) still faces challenges such as market barriers and limited commercial availability, we focus on V1G (unidirectional EV charging) in this study. However, EV discharging functionality is supported in the optimization framework.

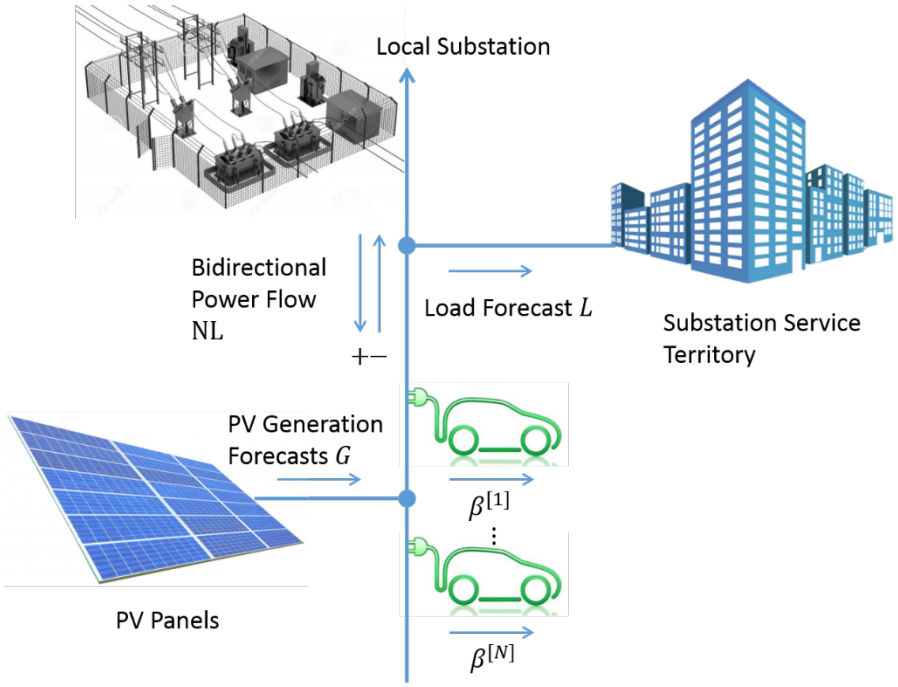

Figure 2: Notation and topology of the proposed optimization problem.

From Figure 2, the following power balance between the four power variables always holds true:

$$\mathrm{NL} = L + \boldsymbol{\beta} - G, \tag{1}$$

where EV charge power $\boldsymbol{\beta} = [\beta^{[1]} \dots \beta^{[N]}]$. As we are interested in a day-ahead optimal valley filling solution, the total length of the planning horizon is 24 hours as in $s = 96$ steps at a temporal resolution Δ of 15 min (0.25 h), consistent with the USI forecast horizon. The time index $T_k = k\Delta$. The power variables in Eqn. 1 at each time index represent the average power output over the period from a time index ahead to present, expressed as $((k-1)\Delta,\ k\Delta)$, where $k \in [1 \dots s]$. For example, the power balance at the first time index T_1 considers the average power output between midnight $0\Delta = 00{:}00$ h and $1\Delta = 00{:}15$ h. Refer to Figure 4 for detailed illustration of planning horizon, temporal resolution and time step.

Figure 3 illustrates the schematic overview of the proposed study. The study solves the valley filling optimization problem with individual input of four solar forecast scenarios (section 2.2) G_{p}, $G_{\mathrm{p+USI}}$, $G_{\mathrm{p+perfect}}$, and G_{perfect}, and compares the resulting bidirectional net load NL_{p}, $\mathrm{NL}_{\mathrm{p+USI}}$, $\mathrm{NL}_{\mathrm{p+perfect}}$, and $\mathrm{NL}_{\mathrm{perfect}}$ respectively.

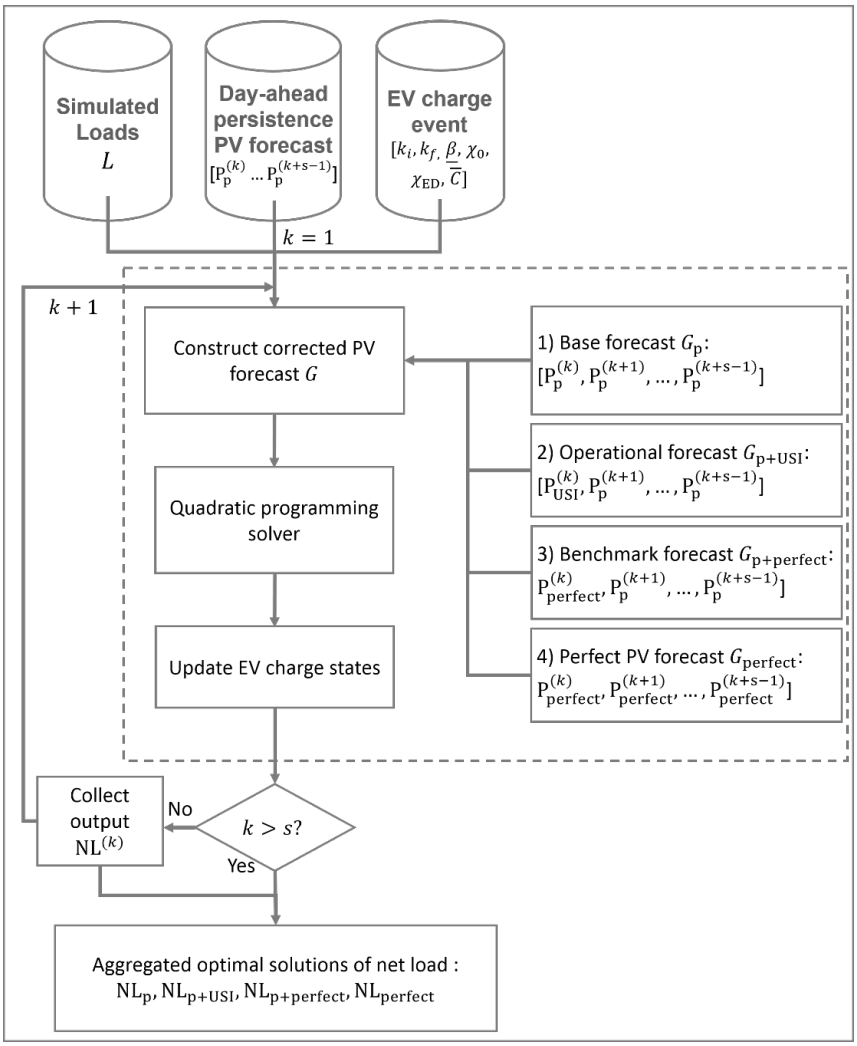

Figure 3: Flowchart of the proposed corrective approach. Refer to Table A-1 for the EV charge events.

3.2 Mathematical Formulation of the Optimization Algorithm

Battery scheduling to reduce peak load and minimize energy bills has been implemented through a variety of optimization algorithms [42]. Considering potential future applications of implementing financial incentives and prioritizing EVs, we prefer a framework which naturally supports weighting different objectives. Therefore, quadratic programming (QP) is selected owing to its flexibility:

$$\min_x h(x - f)^2, \qquad 2$$

where x is a vector of grid net load NL and EV charge power β of each EV (see Eqn. 6), and h is the corresponding matrix of weighting factors. While the weighting factor is not activated in this paper, it enables future implementation of economic objectives that allow trade-off between the decision variables (e.g., price, charge power). Thus, the weighting matrix h is set to a $(1 + N)s \times (1 + N)s$ matrix with an $s \times s$ identity matrix $\boldsymbol{I_s}$ included in the top left corner for grid and zero elsewhere for EV.

$$h = \begin{bmatrix} \boldsymbol{I_s} & \dots & 0 \\ \vdots & \ddots & \vdots \\ 0 & \dots & 0 \end{bmatrix} \in \mathbb{R}^{[(1+N)s \times (1+N)s]} \qquad 3$$

In Eqn. 2, f is a vector composed of the preferred grid net load profile followed by preferred EV charge power. It defines the power target for the objective function. Ideally, the optimized grid net load profile should be a flat line in case of perfect forecasts (i.e. load forecast and solar forecast) and unrestricted EV availability. However, as discussed earlier, real solar forecasts have

errors, and also EV availability can be restricted depending on EV owner's work schedule. The resulting mismatch between the EV energy demand and the energy valley magnitude forces the optimized net load to deviate from a flat line (see Section 4). The preferred grid net load f should therefore be dynamically updated to align the future charge schedule with the remaining PV generation and EV charging needs, and is defined as

$$f_{(k)} = \begin{bmatrix} \boldsymbol{r} \\ 0 \\ \vdots \\ 0 \end{bmatrix} \in \mathbb{R}^{(1+N)s}, \qquad 4$$

where $\boldsymbol{r} = [r, \dots r]^T \in \mathbb{R}^s$ is the grid net load target with identical scalar element r, which is determined from the expected net load $(L - G)$ and the cumulative EV energy demand (χ_{ED}) for the time period from the current time step (t_k) to when the last EV disconnects (t_{end}):

$$r = \frac{\Sigma_{t_k}^{t_{\mathrm{end}}} L - G + \chi_{\mathrm{ED}}}{t_{\mathrm{end}} - t_k}. \qquad 5$$

$\boldsymbol{r}$ is not computed before the first EV connects (t_{start}) and after the last EV disconnects (t_{end}), i.e. $t_{\mathrm{end}} > t_k > t_{\mathrm{start}}$, because we perform valley filling only during the EV layover time. As $\boldsymbol{r}$ assumes equal EV availability and charge rate capacity from present to the departure time of the last EV, the final optimized net load is expected to deviate slightly from the dynamic $\boldsymbol{r}$ even with a perfect solar forecast. The deviation is caused by EV departures that limit the available charging capacity. A detailed discussion is provided in Section 4. The remaining elements in Eqn. 4 are set to zero, indicating that individual EVs can draw power up to the maximum charge power capacity.

To proceed, x in Eqn. 2 is the decision variable consisting of temporal aggregated grid power load and all EV charge power.

$$x = \begin{bmatrix} \mathrm{NL} \\ \beta^{[1]} \\ \vdots \\ \beta^{[N]} \end{bmatrix} \in \mathbb{R}^{(1+N)s} \qquad 6$$

$\mathrm{NL} = [\mathrm{NL}_{(1)}, \dots, \mathrm{NL}_{(k)}]^T$ and EV charge power follows $\beta^{[N]} = [\beta_{(1)}^{[N]}, \dots, \beta_{(k)}^{[N]}]^T$ where $k \in [1, \dots, s]$, N is the number of EVs, and parenthesis () indicate the time index.

The charge power β of each EV in Eqn. 6 is subject to the following five constraints (i.e. Eqns. 7-11). First, the EV charge power is limited to its maximum charge capacity. Because discharging is not considered, the EV charge rate constraint for all time steps k is:

$$0 \le \beta_{(k)} \le \overline{\beta}, \qquad k \in [1, \dots, s] \qquad 7$$

where $\overline{\beta}$ is the maximum of the rated charge capacity of the battery or charging station.

Second, the state of charge (SOC) of the battery is constrained by:

$$\underline{C} \le \chi_0 \cdot \overline{C} + \sum_{k=1}^{s} \beta_{(k)} \cdot \Delta \le \overline{C}, \quad k \in [1, \dots s] \qquad 8$$

where χ_0 is the initial SOC in %, $\overline{C}$ is maximum SOC conventionally defined as the EV battery capacity and the minimum SOC $\underline{C}$ is assumed to be 0. The EV battery capacity is assumed to equal the amount specified by the vehicle manufacturer. Battery degradation is assumed to be negligible.

Third, the charging has to occur within the constraints of the EV layover time. If the EV connects at time index k_i, no charging can occur during the period $[T_1\ T_{k_i}]$. In other words, EV charge power equals to 0 prior to connecting at $k = k_i$:

$$\sum_{k=1}^{k_i} \beta_{(k)} \cdot \Delta = 0. \qquad 9$$

Fourth, similarly given EV departure time index k_f, the EV battery charge is constrained to 0 after disconnecting at $k = k_f$:

$$\sum_{k=k_f}^{s} \beta_{(k)} \cdot \Delta = 0. \quad (10)$$

Last, the power supplied to the EV during the layover period equals the energy requested by the EV owner. We assume that all EV owners request a fully charged battery.

$$\sum_{k=1}^{s} \beta_{(k)} \cdot \Delta = \chi_{\mathrm{ED}} \quad (11)$$

3.3 Receding Horizon Optimization Algorithm

To support the proposed corrective approach, a RHC algorithm is required [43-45]. The RHC algorithm modifies the control action with respect to predicted solar energy generation while satisfying constraints over a time window of fixed length 24 h. We use a moving time window resembling the receding horizon mechanism of RHC. The simulations are initialized at midnight and the time window moves forward one step at a time, as presented in Figure 4.

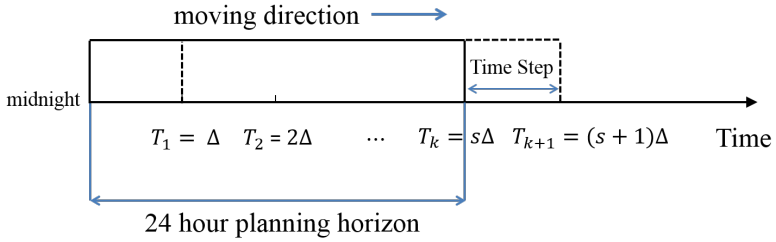

Figure 4: Illustration of receding horizon time window. Refer to Section 3.1 for definitions of the notations.

The iterations in RHC demand a fast optimization solver and real time application can be limited by the number of constraints and EVs. With 31 EVs, each iteration takes 1.5 s on an Intel I5 workstation, and a full day completes in 2.5 min. The computation cost scales with the number of variables (i.e., the number of EVs).

3.4 Forecast and Valley Filling Benchmark

The valley filling performance is evaluated as follows. The accuracy of the solar forecasts is characterized by nRMSD e^G, which is the root mean square difference normalized by the average solar power measurements:

$$e^G(\mathrm{day}) = \frac{\sqrt{\frac{1}{s}\sum_{k=1}^{s}[\mathrm{G}_{\mathrm{forecast}}(k) - \mathrm{G}_{\mathrm{perfect}}(k)]^2}}{\frac{1}{s}\sum_{k=1}^{s}[\mathrm{G}_{\mathrm{perfect}}(k)]} \times 100\%. \quad (12)$$

Similarly, the nRMSD for optimized net load e^{NL} is defined as:

$$e^{\mathrm{NL}}(\mathrm{day}) = \frac{\sqrt{\frac{1}{t_{\mathrm{end}} - t_{\mathrm{start}}}\sum_{k=t_{\mathrm{start}}}^{t_{\mathrm{end}}}[\mathrm{NL}_{\mathrm{imperfect}}(k) - \mathrm{NL}_{\mathrm{perfect}}(k)]^2}}{|\max(\mathrm{NL}_{\mathrm{perfect}}(k))|} \times 100\%. \quad (13)$$

Thus, the nRMSD of valley filling using imperfect solar forecasts $\mathrm{NL_p}$, $\mathrm{NL_{p+USI}}$, and $\mathrm{NL_{p+perfect}}$ can be evaluated by $e^{\mathrm{NL}}_{\mathrm{p}}$, $e^{\mathrm{NL}}_{\mathrm{p+USI}}$, and $e^{\mathrm{NL}}_{\mathrm{p+perfect}}$ respectively. Note that only the net load at the first time step (15 min) of all time windows is evaluated in Eqn. 13 which means that at each index k, the solar forecasts for 15+ min horizon do not influence e^{NL}.

We also evaluate the net load variability as the average square of the deviation between the optimized net load and the idealized valley filling result. The resulting metric σ^{NL} is the standard deviation of the optimized net load:

$$\sigma^{\mathrm{NL}}(\mathrm{day}) = \sqrt{\frac{1}{N}\sum_{t_{\mathrm{end}}}^{t_{\mathrm{start}}} [\mathrm{NL}(k) - \overline{\mathrm{NL}}]^2}, \qquad 14$$

where $\overline{\mathrm{NL}}$ is the average net load from t_{start} to t_{end}, and N is the number of time indices in between. Small σ indicates smoother net load profiles, and $\sigma = 0$ indicates a completely flat net load profile. The net load standard deviations after valley filling using solar forecasts $\mathrm{NL_p}$, $\mathrm{NL_{p+USI}}$, $\mathrm{NL_{p+perfect}}$, and $\mathrm{NL_{perfect}}$ are evaluated by $\sigma_{\mathrm{p}}^{\mathrm{NL}}$, $\sigma_{\mathrm{p+USI}}^{\mathrm{NL}}$, $\sigma_{\mathrm{p+perfect}}^{\mathrm{NL}}$, and $\sigma_{\mathrm{perfect}}^{\mathrm{NL}}$, respectively. Eqns. 13 and 14 are evaluated only during the maximum layover period (i.e. from t_{start} to t_{end}) when the energy valley can be filled.

4. Results and Discussion

4.1 Case Study

The methodology discussed in Section 3.3 is first applied to a single day with the perfect forecast scenario G_{perfect}. Apr 1, 2013 was a day with broken cumulus clouds, producing high PV output variability. Figure 5 shows the valley filling results by smart charging EV 1 and EV 3 defined in Table A-1. The algorithm dynamically schedules charging during energy valleys while obeying all constraints. Specifically, the grid net load profile on the top (subtracting actual PV power G_{perfect} from the feeder load profile L) shows an energy valley during midday interrupted by episodes of cloud cover. The area between blue and red indicates the share of the energy valley that is absorbed by coordinating charging of 2 EVs.

EV 3 has a small energy demand of 7.7 kWh, but the layover period of 9 hours is comparably long since EV 3 only requires 2 h 20 min of charging at the highest charging rate to reach full charge. Thus, the algorithm can schedule charging to occur only during the four major energy valleys (clear periods during midday) while reducing charging power to zero in cloudy conditions and at the beginning and end of the day. EV 3 is fully charged 2 h prior to its planned departure.

On the contrary, EV 1 has much less charging flexibility with a larger energy demand (76.5 kWh or 7 h 39 min of charging at maximum capacity), which is spread over a similar layover period of 9 hours 40 min. Thus, the algorithm has limited flexibility (2 hours) to shift the battery charge schedule and/or reduce the charge rate. EV 1 connects to charge at 08:00 PST, and charging occurs from 08:15 PST when PV generation starts to depress the net load profile. The 2 h flexibility is used to charge at a rate below the maximum capacity from 08:15 to 13:30 PST. By lowering the charge rate, the algorithm shifts EV charging from times of relatively large net load to times with a larger energy valley later in the day. The algorithm boosts charge power of EV 1 to maximum capacity after 13:30 PST so that EV 1 can reach full charge right at its planned departure. Note that limited EV flexibility prevents the algorithm from completely shifting the EV charging to periods with larger energy valleys and it schedules charging also during off-peak solar generation (08:00 – 10:45 PST).

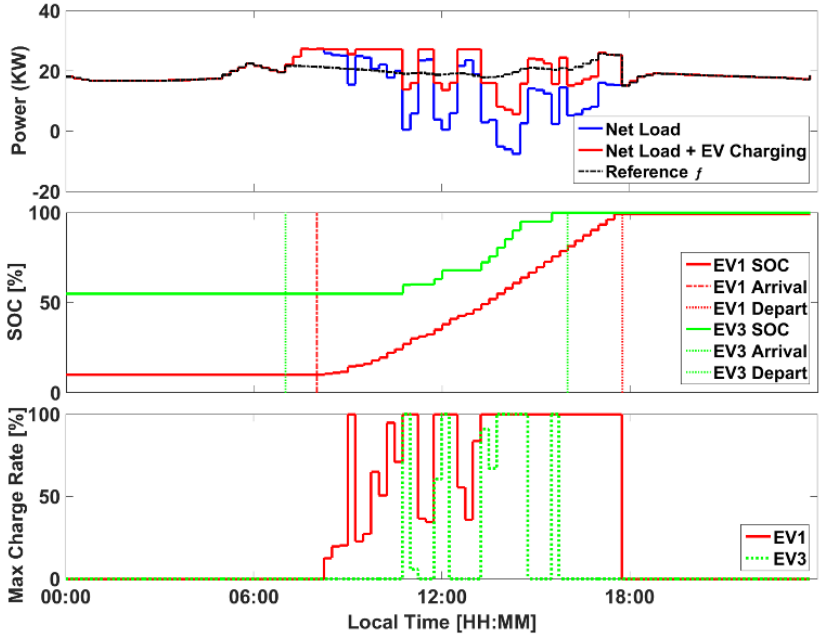

Figure 5: Sample optimized EV charge schedule for valley filling with 2 EVs. Top: Original grid net load profile showing an energy valley (blue), filling the valley towards a reference power (*f*, black) yields optimized net load (red). The PV output profiles are scaled down by a factor of 260x to create a reasonable energy valley for just two EVs. Middle: EV state of charge in %. Colors distinguish EV with their arrival time (dashed) and departure time (dotted). Bottom: EV charge power normalized by its maximum charge capacity.

For this case, the power reference is unachievable due to the small number of EVs and restricted charge schedule for EV 1. But the algorithm's functionality and ability to reduce net load variability by shifting the charge schedule with respect to the energy valley availability is confirmed.

4.2 Monthly Results and Statistics of Forecast Error Correction

Now we consider a full month, 31 EVs (Table A-1 in the Appendix), and four solar forecast scenarios. For readability, only scenario NL_{p+USI} is presented in Figure 6. On most days, valleys are completely filled, and optimized net load is closely aligned with the reference *f* indicating that the method works as designed. On clear days (e.g., Apr 21 – Apr 23), the energy valley is sufficiently large to charge all EVs, yielding a flat net load. On partly cloudy days (e.g., Apr 1 and Apr 4), solar variability is large, and less energy is available in the valley, resulting in increased and fluctuating optimized net load.

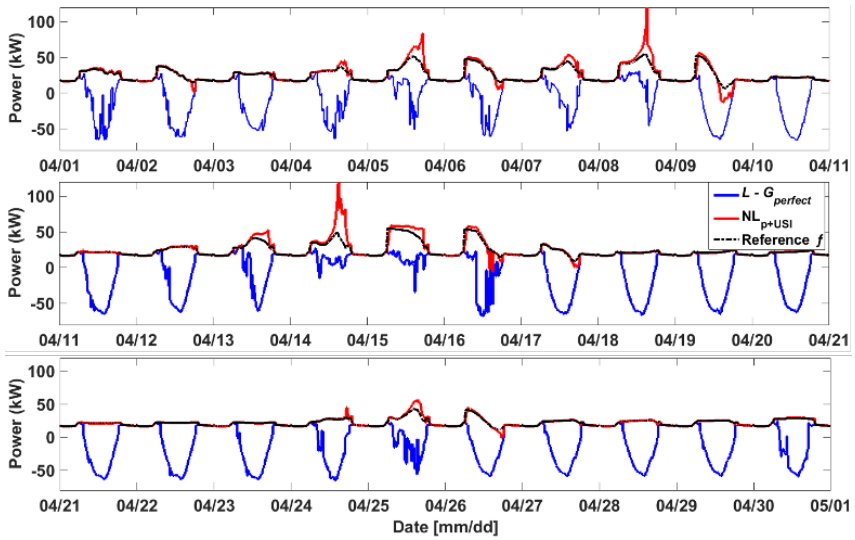

Figure 6: Results for one month of valley filling with forecast errors corrected by USI (using G_{p+USI}). The original grid net load without EV (blue) is flattened by scheduling EV charging to achieve a preferred net load profile (black), resulting in reduced net load variability (red).

Table 2 summarizes the monthly performance and a detailed day-by-day performance comparison is presented in Figure 7. The statistics of PV forecast errors and resulting valley filling performance are further investigated in the following sub-sections.

Table 2: Monthly summary of solar forecasts accuracy and optimized net load variability under different forecast error scenarios.

	Persistence Forecast	USI Forecast	NL_p	NL_{p+USI}	$NL_{p+perfect}$	$NL_{perfect}$
nRMSD e [%]	68.2	37.2	23.1	17.5	14.1	N/A
Std. σ [kW]	N/A	N/A	11.7	8.8	7.3	1.1

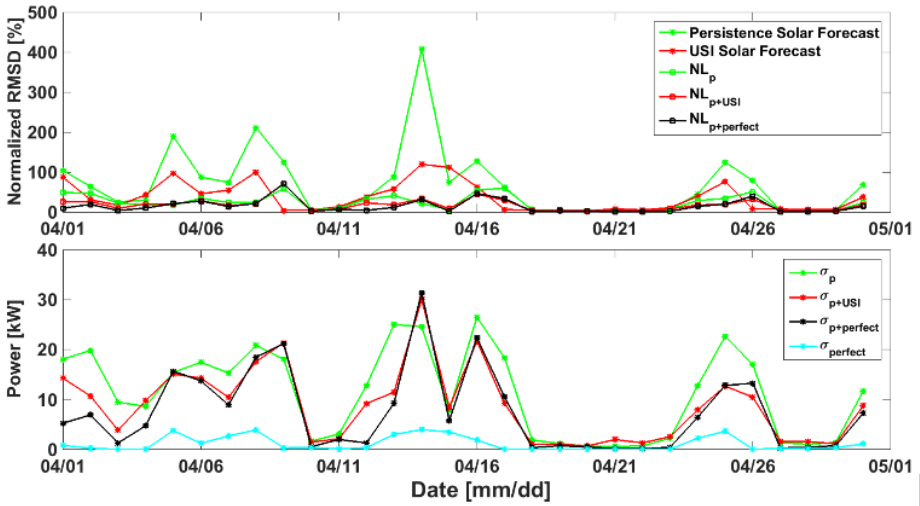

Figure 7: Monthly comparison of nRMSD (top, Eqn. 13) and net load variability (bottom, Eqn. 14). Line colors distinguish solar forecasts scenarios (Section 2.1). See Table A-2 for the same information in tabular form.

4.2.1 Persistence and USI PV Forecast Accuracy

Overall, the USI solar forecast outperforms 24-hour persistence on 17 out of 30 days. While the persistence forecast outperforms USI by an average nRMSD of 6.2 percentage points (30.8%) on the remaining 13 days, the USI solar forecast lowers monthly average nRMSD by 31.0 percentage points (45.4%) placing it about halfway between persistence and perfect forecast. In general, the solar forecast results confirm our expectation that correcting persistence forecast by USI forecast reduces forecast error.

4.2.2 Valley Filling with USI Forecast Correction

Overall, NL_{p+USI} delivers monthly nRMSD and σ averages of 17.5% and 8.8 kW, which are 24.2% and 24.8% below NL_p, respectively. The optimization for NL_p and NL_{p+USI} forecasts performs similarly for mostly clear days and errors are small; specifically, both NL_p and NL_{p+USI} yield low error and variability averages less than 5.0 percentage point and 2.0 kW, respectively. On the 15 partly cloudy days NL_{p+USI} outperforms NL_p by 33.0% and 32.7%. While NL_{p+USI} performs worse than NL_p on some of the days when sky conditions in present day significantly differ from a day earlier (Apr 5, 8, 9, 14, 16, 25 and 26, see Section 4.3), the average error reductions of NL_{p+USI} over NL_p on these days are still 7.9% and 11.2% for nRMSD and σ, respectively. Note that the large improvement in solar forecast accuracy by the USI over persistence forecast (45.4%) does not translate to an equal improvement in optimized net load variability, which will be discussed in Section 4.4.

4.2.3 Valley Filling with Perfect Forecast Correction

The error reductions by $NL_{p+perfect}$ over NL_{p+USI} are relatively smaller (19.4% and 17.0% less with respect to nRMSD and σ). The fact that NL_{p+USI} is closer to $NL_{perfect}$ than NL_p demonstrates the feasibility of operational forecast deployment of USI forecasts.

Valley filling with perfect 24-hour forecasts performs the best as expected with monthly average σ_{perfect} of 1.1 kW. Although $\text{NL}_{\text{perfect}}$ may be expected to be perfectly flat with zero variance, the optimized net load in the morning and evening usually ramps up and down over a finite time period (e.g. cyan in Figure 8a), causing non-zero variance. This ramp is a result of limited EV availability just after the first EV connects and before the last EV disconnects. For example, just the first EV by itself is not capable of dispatching sufficient charging power to follow a desired power r that is determined by spreading the energy of all EVs over the entire charging interval.

4.3 Characterization of Solar Forecast Error Impacts

The proposed receding horizon optimization with forecast error corrected by more accurate short-term forecasts ($G_{\text{p+USI}}$) is generally effective in filling the energy valley. Exceptions are observed on Apr 5, 8, 9, 14, 16, 25, and 26 with a large peak in the optimized net load (Figure 6). To understand the challenges of the optimization on those days and further investigate the negative impact of solar forecast errors, we showcase a detailed example for Apr 14 in Figure 8.

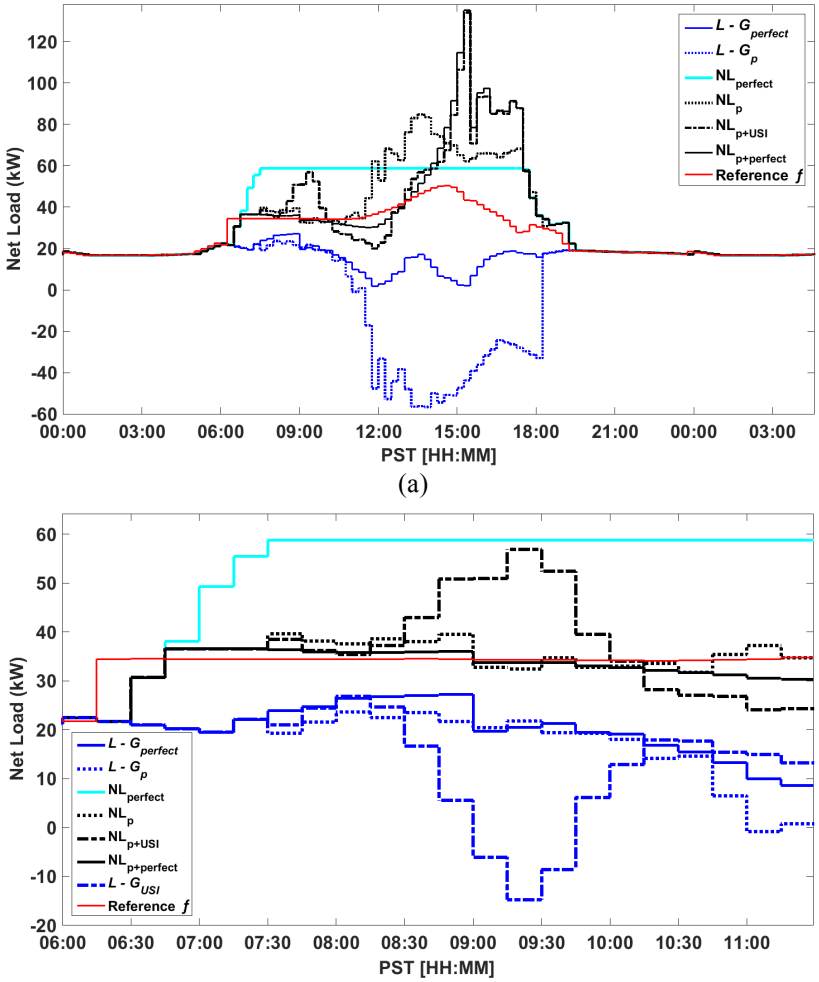

Figure 8: Comparison of valley filling performance using different solar forecasts (i.e. G_{p}, $G_{\text{p+USI}}$, $G_{\text{p+perfect}}$, G_{perfect}) on Apr 14 (a) and zooming in to the period from 06:00 to 11:00 PST (b). Line styles distinguish solar forecast scenarios, and blue and black colors differentiate net load with and without EV charging, respectively. The perfect net load forecast (load minus perfect PV forecast, solid blue) yields the ideal optimized net load (cyan).

On Apr 14, the baseline forecast G_{p} predicts large PV generation and net load valley (dotted blue) while this day is actually overcast with limited excess energy (solid blue). Between 06:30 PST and 12:00 PST, operating under the assumption of persistence forecast for >15 minute horizons, the algorithm expects a large energy valley later in the day. Therefore, it delays most of the non-critical EV charging while maintaining a flat net load profile. Because G_{p} is close to G_{perfect} (i.e. dotted blue follows solid blue) until 12:00 PST, the EV charging is on an ideal trajectory; if the excellent accuracy of G_{p} had continued, the valley filling would have flattened the net load across the day. However, after 12:00 PST, G_{p} deviates from G_{perfect}. Even though the energy valley is in fact not available, the forecasts still predicts an abundant energy valley from 12:00 until 18:00 PST, thus

EV charging is postponed to that time. The charge rate for each interval roughly equals the difference between f and G_{p}. Therefore, the variations in the resulting valley filling scenario NL_{p}, mirror the difference between perfect net load forecast ($L - G_{\mathrm{perfect}}$) and persistence net load forecast ($L - G_{\mathrm{p}}$). The peak error in G_{p} corresponds to the largest net load peak in NL_{p} at about 13:30 PST.

On this day, the day-ahead forecast error correction actually worsens the net load variability. Starting from 12:00 PST, when G_{p} is replaced with the USI forecast G_{USI} or the perfect forecast G_{perfect} for the next 15 min, the energy valley forecasted by G_{p} for the next 15 min is no longer available. Therefore, the optimization delays scheduling EV charging at the present time step, because it still expects an energy valley 15+ minutes from now (where G_{p} has not been updated yet). At the next time step, the situation is similar and EV charging is again rescheduled for later. Thus, non-critical EV charging is delayed until 13:30 PST when a number of early-departure EVs start to approach their charge time limit. Since those EVs must start to charge at their maximum charge capacity immediately to be fully charged (refer to Eqn. 11 for the constraint) by their planned departure time, the algorithm has to schedule those EVs immediately, independent of load flattening objectives, causing a steep net load rise. After 16:00 PST, another set of EVs approach their charge time limit, resulting in a second peak. Overall the resulting net load profiles $\mathrm{NL}_{\mathrm{p+USI}}$ and $\mathrm{NL}_{\mathrm{p+perfect}}$ resemble that of a maximum delay strategy, causing most EVs to concurrently charge at their full charge rate. On the contrary, operating under G_{p} only causes the algorithm to allocate the charge power more equally across the afternoon, reducing the peak in the corresponding optimized net load profile NL_{p} (dotted black). Consequently NL_{p} shows lower σ (24.6 kW) than $\mathrm{NL}_{\mathrm{p+USI}}$ and $\mathrm{NL}_{\mathrm{p+perfect}}$ (30.0 kW, 30.4 kW, Table A-2). Lastly, the perfect forecast G_{perfect} (solid blue) yields a perfect valley filling $\mathrm{NL}_{\mathrm{perfect}}$ (cyan) during the EV layover time ($\sigma \cong 0$).

The subtle difference between the impacts of the three imperfect solar forecast inputs G_{p}, $G_{\mathrm{p+USI}}$ and $G_{\mathrm{p+perfect}}$ on the resulting net load profiles is further analyzed in Figure 8b by zooming into the period from 06:00 to 11:00 PST. Before 07:30 PST, the lack of PV power output makes all optimized net load profiles identical. However, the algorithm still schedules to charge early-arrival EVs because of overall insufficient energy valley across the day, pushing the grid net load upward. Later on at 07:30 PST, PV starts generating power and because G_{p} and G_{USI} forecast errors differ, G_{p}, $G_{\mathrm{p+USI}}$ and $G_{\mathrm{p+perfect}}$ exhibit small optimized net load valleys. The original net load differences (all in blue) carry through to the resulting optimized net load profiles NL_{p}, $\mathrm{NL}_{\mathrm{p+USI}}$ and $\mathrm{NL}_{\mathrm{p+perfect}}$ (all in black). From 08:30 to 10:30 PST, erroneous G_{USI} causes a predicted net load valley (dashed blue), so the algorithm schedules EVs to charge, producing a net load peak (dashed black) at 09:00 PST. After 10:30 PST, the net load peak starts to diminish as G_{USI} starts to mostly follow G_{perfect} again. During the entire morning the valley filling resulting from the three imperfect solar forecasts deviates significantly from the idealized result (cyan). If the algorithm understood the true solar generation from the beginning of planning horizon, it would schedule the charging much earlier in the day and flatten the entire net load profile. This comparison further demonstrates the negative impact of forecast errors on flattening grid net load.

Furthermore, the day discussed in Figure 8 illustrates the relationship between day-to-day change in sky conditions (larger and more auto-correlated error in base forecast) and net load peaks (refer to Figure 6 and Appendix Table A-2). On Apr 14 (the first of two consecutive overcast days of Apr 14 and Apr 15), the persistence solar forecast error, e_{p}^{G} is large (241% greater than $e_{\mathrm{p+USI}}^{G}$) because cloud conditions change from a clear day with few thin cirrus (Apr 13) to an overcast day with thick clouds. The high persistence error results in a large evening peak in optimized net load with $\sigma_{\mathrm{p}}^{\mathrm{NL}}$ of 24.6 kW. On Apr 14, correcting base forecast by better sky imagery forecasts actually worsens the net load variability ($\sigma_{\mathrm{p+USI}}^{\mathrm{NL}} = 30.0$ kW). However, on the second overcast day (Apr 15), the persistence forecast performs better (74 percentage points), consequently both NL_{p} and $\mathrm{NL}_{\mathrm{p+USI}}$ performs better with $\sigma_{\mathrm{p}}^{\mathrm{NL}}$ and $\sigma_{\mathrm{p+USI}}^{\mathrm{NL}}$ reduced to 7.8 kW and 8.4 kW, and large net load peaks are eliminated. Similar load peaks occur on other days with changes in day-to-day sky conditions. If the present day is cloudier than the previous day, the day-ahead persistence forecast will cause the algorithm to push the EV charging peak forward (Apr 5, Apr 8, Apr 14, Apr 25). Conversely, if the present day has less clouds than the previous day, the persistence forecast will push the peak backward (Apr 9, Apr 16, Apr 26).

4.4 Discussion and Potential Limitations

The autocorrelation of the forecast error, i.e. persistent over- or underforecasts over a few hours, causes the largest deviations in optimized net load with erroneous forecasts from the optimized net load with perfect forecasts. Section 4.2 verifies that the forecast error structure is an important determinant of optimized net load variability. For example, as observed in Figure 8, if clear sky is predicted on a cloudy day, then the midday net load depression is over-forecast and EV charge schedule in the morning would be unnecessarily delayed. In the valley filling literature, forecast errors have mostly been modeled through statistical approaches. When forecast errors are sampled from a distribution such as in [11], then the forecast error autocorrelation

is around zero making it more likely to happen that an overforecast during one interval is balanced by an underforecast in the following intervals. While forecast errors with zero autocorrelation will result in temporary small deviations in optimized net load, these idealistic forecast errors are unlikely to produce the cumulative effects that results in dramatic optimized net load deviations. This means that simple statistical models in the valley filling literature degrade the autocorrelation of forecast data, resulting in optimistic solutions.

The proposed corrective approach and the use of the realistic forecast data reveal that the deviation of practical valley filling performance from the ideal valley filling is tied to three conditions: 1) EV charging flexibility. Because of the constraint to satisfy EV energy needs, EVs with short layover periods and large energy needs limit scheduling flexibility. EV charging inflexibility prevents the load flattening objectives from being fully met even with perfect forecasts. 2) Accuracy of day-ahead forecasts. Large changes in cloud conditions on two consecutive days worsen day-ahead persistence forecasts, leading to large peaks in optimized net load. 3) Accuracy of the short-term forecast. Reducing forecast error by short-term forecast generally yields better valley filling performance (Figure 7).

For a more accurate valley filling problem, the following improvements should be considered. 1) Accelerated adoption of EVs is needed to provide adequate amounts of controllable loads. In this work, the load and PV generation data had to be scaled down significantly for 31 EVs to just fully balance the energy valley. More financial incentives are necessary to encourage adoption of the smart charging standards. 2) The load demand timeseries was simulated through an energy simulation tool because feeder load data are typically not published by distribution system operators. As the simulated data may lack real power variability, the value of smart charging may be higher than shown in this paper. 3) Last, integrating economic incentive and EV battery aging models in the framework can make the study more comprehensive.

5. Conclusions

Electric utilities are experiencing unprecedented growth in the adoption of grid-connected solar PV. Solar forecasts are essential to the integration of PV and balancing supply and demand. This paper successfully demonstrates a corrective approach to mitigate negative impacts of day-ahead forecast errors using a sky imager based forecasting technique. The proposed methodology was tested against 24-hour persistence solar forecasts with one month of PV generation and substation load data. We showcase smart EV scheduling as a promising mechanism for absorbing the net load depression created by high PV penetration. This study differs from the literature regarding the forecast error modeling as we use real data to preserve autocorrelation characteristics of forecast errors and avoid statistical approximations. Our primary findings are:

i. Realistic forecast errors prevent the optimal charge strategy from flattening the net load.

ii. More accurate short-term forecasts input to the corrective receding horizon optimization reduce net load variability.

Correcting the day-ahead persistence forecasts by sky imager forecasts for 15 min horizons reduces net load variability on 20 out of 30 days, and presents comparable results on the remaining days which are mostly clear. On average over the month, the standard deviation of the net load profile is reduced by 24.7%. On the 15 partly cloudy days, the short-term forecast correction reduces net load variability by 32.7%. On clear days, the proposed correction scenario optimizes net load variability to be below 3.0 kW given a scaled energy valley of 50 kW, which is only 1.5 kW worse than for a perfect forecast correction.

For future work, we will use real EV charge events and EV charging forecasts. More accurate day-ahead solar forecasts generated by numerical weather prediction and machine learning techniques will also be pursued. Because sub-optimal charging strategies worsen the net load variability, understanding possible variations associated with forecast errors around a single deterministic strategy will be of great benefit to grid operators. Finally, a stochastic optimization framework that integrates probabilistic PV forecast and EV availability and demand forecasts allows a more robust valley filling.

Appendix:

Table A-1: Daily EV charging events database. Refer to Section 3 for a detailed definition of the variable names.

ID and EV Model	Arrival Time k_i [PST]	Departure Time k_f [PST]	Charge Rate capacity $\underline{\beta}$ [kW]	Initial State of Charge χ_0 [%]	Energy Demand χ_{ED} [kWh]	Battery Capacity $\overline{C}$ [kWh]
1: Tesla Model S	08:00	17:40	10	10	76.5	85
2: Toyota Prius	06:10	14:35	3.3	5	3.8	4
3: Chevy Volt	07:00	16:00	3.3	55	7.7	17
4: Toyota Prius	06:10	15:40	3.3	80	0.8	4
5: Nissan Leaf	06:30	16:45	6.6	95	1.2	24
6: Chevy Volt	08:30	19:15	3.3	15	14.5	17
7: Chevy Volt	08:00	17:10	3.3	60	6.8	17
8: Nissan Leaf	07:10	15:10	6.6	50	12	24
9: Toyota Prius	09:10	17:10	3.3	40	2.4	4
10: Toyota Prius	06:10	14:35	3.3	20	3.2	4
11: Chevy Volt	07:30	17:30	3.3	80	3.4	17
12: Toyota Prius	07:20	15:45	3.3	35	2.6	4
13: Toyota Prius	08:20	18:15	3.3	55	1.8	4
14: Nissan Leaf	08:20	16:40	6.6	20	19.2	24
15: Tesla Model S	06:50	17:20	10.0	65	29.8	85
16: Chevy Volt	07:30	16:10	3.3	30	11.9	17
17: Ford Fusion Energi	07:30	15:40	3.3	70	2.1	7
18: Toyota Prius	08:00	16:25	3.3	70	1.2	4
19: Tesla Model S	08:10	17:30	10	75	21.3	85
20: Toyota Prius	08:10	17:10	3.3	50	2	4
21: Nissan Leaf	07:00	15:40	6.6	10	21.6	24
22: Chevy Volt	08:00	18:00	3.3	30	11.9	17
23: Tesla Model S	08:00	17:15	10.0	90	8.5	85
24: Toyota Prius	06:40	15:50	3.3	20	3.2	4
25: Nissan Leaf	06:30	16:55	6.6	85	3.6	24
26: Tesla Model S	07:30	16:00	10.0	60	34	85
27: Tesla Model S	09:10	18:55	10.0	10	76.5	85
28: Ford Fusion Energi	07:10	16:50	3.3	50	3.5	7
29: Nissan Leaf	07:50	16:35	6.6	15	20.4	24
30: Chevy Volt	06:50	16:00	3.3	80	3.4	17
31: School Bus	11:00	16:15	70.0	50	57.5	115

Table A-2: Normalized RMSD for solar forcast (e^{G}) and optimized net load (e^{NL}), and standard deviation of the optimized net load σ^{NL} under scenarios of base forecast, operational forecast, benchmark forecast, and perfect forecast. Superscripts indicate the type of validations and subscripts indicate the solar forecasts scenarios used in the valley filling problem.

Date MM/DD/YY	e^{G}_{p} [%]	e^{G}_{USI} [%]	$e^{\mathrm{NL}}_{\mathrm{p}}$ [%]	$e^{\mathrm{NL}}_{\mathrm{p+USI}}$ [%]	$e^{\mathrm{NL}}_{\mathrm{p+perfect}}$ [%]	$\sigma^{\mathrm{NL}}_{\mathrm{p}}$ [kW]	$\sigma^{\mathrm{NL}}_{\mathrm{p+USI}}$ [kW]	$\sigma^{\mathrm{NL}}_{\mathrm{p+perfect}}$ [kW]	$\sigma^{\mathrm{NL}}_{\mathrm{perfect}}$ [kW]
04/01/13	103.8	86.8	49.0	25.0	9.6	18.1	14.3	5.2	0.8
04/02/13	63.6	30.6	46.4	25.9	18.8	19.8	10.7	6.9	0.3
04/03/13	24.6	16.8	22.1	9.0	3.5	9.5	3.8	1.3	0.0
04/04/13	29.9	42.6	17.9	20.0	9.9	8.6	9.8	4.7	0.0
04/05/13	189.1	96.9	16.9	20.0	20.7	15.4	15.1	15.7	3.8
04/06/13	87.1	45.5	34.0	27.9	27.3	17.4	14.3	13.7	1.2
04/07/13	73.9	54.5	23.4	16.0	13.5	15.3	10.4	8.9	2.7
04/08/13	210.9	99.9	23.6	20.4	21.3	20.9	17.6	18.5	3.9
04/09/13	125.5	4.0	58.2	70.0	70.9	18.1	21.3	21.2	0.3
04/10/13	4.4	4.9	4.4	3.9	1.4	1.7	1.5	0.5	0.4
04/11/13	10.9	12.6	9.2	6.5	6.7	3.1	2.1	2.0	0.1
04/12/13	34.2	38.1	31.6	22.6	4.0	12.8	9.2	1.3	0.4

04/13/13	89.0	58.1	40.8	17.9	11.3	25.0	11.5	9.3	3.0
04/14/13	407.4	119.5	20.9	33.0	31.1	24.6	30.0	30.4	4.0
04/15/13	74.1	111.1	6.5	8.2	1.8	7.8	8.4	5.8	3.5
04/16/13	127.4	62.8	54.8	44.4	45.9	26.5	21.7	22.4	1.9
04/17/13	62.7	6.0	59.6	29.3	33.7	18.4	9.2	10.5	0.0
04/18/13	4.0	4.4	5.6	3.9	1.2	1.9	1.1	0.3	0.0
04/19/13	3.4	3.8	3.7	4.1	2.9	1.2	1.1	0.7	0.0
04/20/13	2.9	2.5	2.3	2.6	1.9	0.6	0.7	0.5	0.0
04/21/13	1.8	7.8	1.9	5.9	0.6	0.6	2.0	0.2	0.0
04/22/13	1.6	5.0	2.1	3.9	0.5	0.7	1.3	0.1	0.0
04/23/13	5.6	10.6	6.5	7.4	1.5	2.2	2.6	0.4	0.0
04/24/13	44.8	39.2	28.5	17.3	14.1	12.8	7.9	6.4	2.3
04/25/13	124.4	75.8	33.9	19.0	19.2	22.6	12.7	12.8	3.6
04/26/13	78.3	7.6	50.6	31.7	39.7	17.0	10.5	13.3	0.1
04/27/13	3.1	7.0	3.7	4.6	0.9	1.3	1.6	0.3	0.1
04/28/13	2.7	6.5	2.7	4.3	1.3	1.0	1.6	0.4	0.2
04/29/13	4.7	6.5	3.7	3.5	2.0	1.4	1.1	0.8	0.4
04/30/13	48.7	47.7	29.4	17.5	5.4	14.2	8.5	2.2	0.0
All Days	68.2	37.2	23.1	17.5	14.1	11.7	8.8	7.3	1.1

References

[1] G. Ari, Y. Baghzouz, Impact of high PV penetration on voltage regulation in electrical distribution systems, Clean Electrical Power (ICCEP), 2011 International Conference on, IEEE, 2011, pp. 744-748.
[2] A. Nguyen, M. Velay, J. Schoene, V. Zheglov, B. Kurtz, K. Murray, B. Torre, J. Kleissl, High PV penetration impacts on five local distribution networks using high resolution solar resource assessment with sky imager and quasi-steady state distribution system simulations, Solar Energy 132 (2016) 221-235.
[3] R. Hanna, J. Kleissl, A. Nottrott, M. Ferry, Energy dispatch schedule optimization for demand charge reduction using a photovoltaic-battery storage system with solar forecasting, Solar Energy 103 (2014) 269-287.
[4] M. Delfanti, D. Falabretti, M. Merlo, Energy storage for PV power plant dispatching, Renewable Energy 80 (2015) 61-72.
[5] S. Mazzola, C. Vergara, M. Astolfi, V. Li, I. Perez-Arriaga, E. Macchi, Assessing the value of forecast-based dispatch in the operation of off-grid rural microgrids, Renewable Energy 108 (2017) 116-125.
[6] A.-L. Klingler, L. Teichtmann, Impacts of a forecast-based operation strategy for grid-connected PV storage systems on profitability and the energy system, Solar Energy 158 (2017) 861-868.
[7] P. Coker, J. Barlow, T. Cockerill, D. Shipworth, Measuring significant variability characteristics: An assessment of three UK renewables, Renewable energy 53 (2013) 111-120.
[8] M.Q. Raza, M. Nadarajah, C. Ekanayake, On recent advances in PV output power forecast, Solar Energy 136 (2016) 125-144.
[9] N. Zhang, C. Kang, Q. Xia, J. Liang, Modeling conditional forecast error for wind power in generation scheduling, IEEE Transactions on Power Systems 29(3) (2014) 1316-1324.
[10] V. Mohan, J.G. Singh, W. Ongsakul, An efficient two stage stochastic optimal energy and reserve management in a microgrid, Applied energy 160 (2015) 28-38.
[11] J. Lujano-Rojas, G. Osório, J. Matias, J. Catalão, A heuristic methodology to economic dispatch problem incorporating renewable power forecasting error and system reliability, Renewable Energy 87 (2016) 731-743.
[12] M. Marzband, M. Javadi, J.L. Domínguez-García, M.M. Moghaddam, Non-cooperative game theory based energy management systems for energy district in the retail market considering DER uncertainties, IET Generation, Transmission & Distribution 10(12) (2016) 2999-3009.
[13] Y. Zhang, T. Zhang, R. Wang, Y. Liu, B. Guo, Optimal operation of a smart residential microgrid based on model predictive control by considering uncertainties and storage impacts, Solar Energy 122 (2015) 1052-1065.
[14] E. Scolari, F. Sossan, M. Paolone, Irradiance prediction intervals for PV stochastic generation in microgrid applications, Solar Energy 139 (2016) 116-129.
[15] P. Haessig, B. Multon, H.B. Ahmed, S. Lascaud, P. Bondon, Energy storage sizing for wind power: impact of the autocorrelation of day-ahead forecast errors, Wind Energy 18(1) (2015) 43-57.
[16] W. Wu, K. Wang, B. Han, G. Li, X. Jiang, M.L. Crow, A versatile probability model of photovoltaic generation using pair copula construction, IEEE Transactions on Sustainable Energy 6(4) (2015) 1337-1345.
[17] B. Ngoko, H. Sugihara, T. Funaki, Synthetic generation of high temporal resolution solar radiation data using Markov models, Solar Energy 103 (2014) 160-170.
[18] M. Marzband, N. Parhizi, J. Adabi, Optimal energy management for stand-alone microgrids based on multi-period imperialist competition algorithm considering uncertainties: experimental validation, International transactions on electrical energy systems 26(6) (2016) 1358-1372.
[19] A. Michiorri, J. Lugaro, N. Siebert, R. Girard, G. Kariniotakis, Storage sizing for grid connected hybrid wind and storage power plants taking into account forecast errors autocorrelation, Renewable

Energy 117 (2018) 380-392.
[20] E.N. Martinez, M.J. Koivisto, N.A. Cutululis, P. Sorensen, On the simulation of aggregated solar PV forecast errors, IEEE Transactions on Sustainable Energy (2018).
[21] E. Nuño, M. Koivisto, N. Cutululis, Simulation of regional day-ahead PV power forecast scenarios, PowerTech, 2017 IEEE Manchester, IEEE, 2017, pp. 1-6.
[22] Y. Ru, J. Kleissl, S. Martinez, Storage size determination for grid-connected photovoltaic systems, IEEE Transactions on Sustainable Energy 4(1) (2013) 68-81.
[23] Y. Ru, J. Kleissl, S. Martinez, Exact sizing of battery capacity for photovoltaic systems, European Journal of Control 20(1) (2014) 24-37.
[24] A. Nottrott, J. Kleissl, B. Washom, Energy dispatch schedule optimization and cost benefit analysis for grid-connected, photovoltaic-battery storage systems, Renewable Energy 55 (2013) 230-240.
[25] S. Chen, H.B. Gooi, M. Wang, Sizing of energy storage for microgrids, IEEE Transactions on Smart Grid 3(1) (2012) 142-151.
[26] A.H. Habib, V.R. Disfani, J. Kleissl, R.A. de Callafon, Quasi-dynamic load and battery sizing and scheduling for stand-alone solar system using mixed-integer linear programming, Control Applications (CCA), 2016 IEEE Conference on, IEEE, 2016, pp. 1476-1481.
[27] M. Marzband, A. Sumper, J.L. Domínguez-García, R. Gumara-Ferret, Experimental validation of a real time energy management system for microgrids in islanded mode using a local day-ahead electricity market and MINLP, Energy Conversion and Management 76 (2013) 314-322.
[28] E.L. Ratnam, S.R. Weller, C.M. Kellett, An optimization-based approach to scheduling residential battery storage with solar PV: Assessing customer benefit, Renewable Energy 75 (2015) 123-134.
[29] S. Habib, M. Kamran, U. Rashid, Impact analysis of vehicle-to-grid technology and charging strategies of electric vehicles on distribution networks–a review, Journal of Power Sources 277 (2015) 205-214.
[30] F. Mwasilu, J.J. Justo, E.-K. Kim, T.D. Do, J.-W. Jung, Electric vehicles and smart grid interaction: A review on vehicle to grid and renewable energy sources integration, Renewable and Sustainable Energy Reviews 34 (2014) 501-516.
[31] Z. Wang, S. Wang, Grid power peak shaving and valley filling using vehicle-to-grid systems, IEEE Transactions on power delivery 28(3) (2013) 1822-1829.
[32] P. Denholm, M. O'Connell, G. Brinkman, J. Jorgenson, Overgeneration from Solar Energy in California. A Field Guide to the Duck Chart, National Renewable Energy Lab.(NREL), Golden, CO (United States), 2015.
[33] S. Sae, Electric vehicle and plug in hybrid electric vehicle conductive charge coupler, January, 2010.
[34] S. Stüdli, E. Crisostomi, R. Middleton, R. Shorten, Optimal real-time distributed V2G and G2V management of electric vehicles, International Journal of Control 87(6) (2014) 1153-1162.
[35] T. Wu, Q. Yang, Z. Bao, W. Yan, Coordinated energy dispatching in microgrid with wind power generation and plug-in electric vehicles, IEEE Transactions on Smart Grid 4(3) (2013) 1453-1463.
[36] 2015 General Rate Case APPLICATION, Southern California Edison, 2013.
[37] C.W. Chow, B. Urquhart, M. Lave, A. Dominguez, J. Kleissl, J. Shields, B. Washom, Intra-hour forecasting with a total sky imager at the UC San Diego solar energy testbed, Solar Energy 85(11) (2011) 2881-2893.
[38] C.W. Chow, S. Belongie, J. Kleissl, Cloud motion and stability estimation for intra-hour solar forecasting, Solar Energy 115 (2015) 645-655.
[39] B. Urquhart, M. Ghonima, D. Nguyen, B. Kurtz, C.W. Chow, J. Kleissl, Sky imaging systems for short-term forecasting, Solar Energy Forecasting and Resource Assessment. Elsevier (2013) 195-232.
[40] H. Yang, B. Kurtz, D. Nguyen, B. Urquhart, C.W. Chow, M. Ghonima, J. Kleissl, Solar irradiance forecasting using a ground-based sky imager developed at UC San Diego, Solar Energy 103 (2014) 502-524.

[41] S.J. Kang, J. Park, K.-Y. Oh, J.G. Noh, H. Park, Scheduling-based real time energy flow control strategy for building energy management system, Energy and Buildings 75 (2014) 239-248.
[42] O. Sundstrom, C. Binding, Flexible charging optimization for electric vehicles considering distribution grid constraints, IEEE Transactions on Smart Grid 3(1) (2012) 26-37.
[43] J. Mattingley, Y. Wang, S. Boyd, Receding horizon control, IEEE Control Systems 31(3) (2011) 52-65.
[44] P. Braun, L. Grüne, C.M. Kellett, S.R. Weller, K. Worthmann, Model Predictive Control of Residential Energy Systems Using Energy Storage and Controllable Loads, European Consortium for Mathematics in Industry, Springer, 2014, pp. 617-623.
[45] T. Wang, H. Kamath, S. Willard, Control and optimization of grid-tied photovoltaic storage systems using model predictive control, IEEE Transactions on Smart Grid 5(2) (2014) 1010-1017.